Apparently it is similar factors that make the rate of electron exchange between α-$[P_2Mo_3W_{15}O_{62}]^{6-}$ and α-$[P_2Mo_3W_{15}O_{62}]^{7-}$ even slower than between 18-tungsto complexes.[4] In the 1e blue of α-$[P_2Mo_3W_{15}O_{62}]^{6-}$ the added electron is delocalized only over the three Mo atoms in one cap of the complex.[3a] This probably necessitates Mo cap to Mo cap contact during an electron exchange (which is much less probable than belt to belt contact) and significantly increases the charge density in the 3 Mo cap (again more than the analogous process in the α-$[P_2W_{18}O_{62}]^{6-}$ anion).

Acknowledgment. This research was supported in part by NSF Grant CHE-8406088 and by an instrument grant from the W. M. Keck Foundation.

Registry No. α-$[PW_{12}O_{40}]^{3-}$, 12534-77-9; α-$[PW_{12}O_{40}]^{4-}$, 12534-78-0; α-$[P_2W_{18}O_{62}]^{6-}$, 90751-95-4; α-$[P_2Mo_3W_{15}O_{62}]^{6-}$, 89173-94-4.

Models for Iron-Oxo Proteins. Mössbauer and EPR Study of an Antiferromagnetically Coupled $Fe^{III}Ni^{II}$ Complex

T. R. Holman,[†] C. Juarez-Garcia,[‡] M. P. Hendrich,[‡] L. Que, Jr.,*[,†] and E. Münck*[,‡]

Contribution from the Department of Chemistry, University of Minnesota, Minneapolis, Minnesota 55455, and Gray Freshwater Biological Institute, P.O. Box 100, County Roads 15 and 19, Navarre, Minnesota 55392. *Received February 21, 1990*

Abstract: The bimetallic complex $[Fe^{III}Ni^{II}BPMP(OPr)_2](BPh_4)_2$, where BPMP is the anion of 2,6-bis[(bis(2-pyridylmethyl)amino]methyl]-4-methylphenol, has been synthesized and its structure determined by X-ray diffraction methods as having a (μ-phenoxo)bis(μ-carboxylato) core. The complex crystallizes in the triclinic space group $P\bar{1}$ with cell constants: a = 13.607 (3) Å, b = 13.700 (3) Å, c = 25.251 (7) Å, α = 77.29 (2)°, β = 78.25 (2)°, γ = 61.73 (2)°, Z = 2, V = 4017 (4) Å^3. The metal centers have distinct six-coordinate N_3O_3 environments and are separated by 3.378 (8) Å, similar to related complexes in this series. We have studied the complex with EPR and Mössbauer spectroscopy and magnetic susceptibility. All three techniques establish that the electronic ground state of the complex has spin S = 3/2. For T < 10 K the EPR spectra are dominated by signals of the S = 3/2 multiplet. At higher temperatures, an additional resonance appears. It is centered at g = 4.2 and belongs to an excited multiplet with S = 5/2. We have studied the low-temperature Mössbauer spectra of the complex in external fields up to 6.0 T. Analysis of the well-resolved spectra yields D = 0.7 cm^{-1} and E/D = 0.32 for the zero-field splitting parameters of the S = 3/2 multiplet. Spectra taken in external fields H < 0.5 T reveal that D and E/D are distributed; a simple Gaussian distribution of E/D values fits the data quite well. The Mössbauer spectra show that the Fe^{III} site is high-spin. It follows that the dinuclear complex consists of a ferric ion (S_1 = 5/2) which is antiferromagnetically coupled to a high-spin (S_2 = 1) Ni^{II}. Analysis of the temperature dependence of the g = 4.2 EPR signal yields J = +24 (3) cm^{-1} ($\mathcal{H} = J\mathbf{S}_1\cdot\mathbf{S}_2$); the susceptibility study agrees with this result. Analysis of the ^{57}Fe magnetic hyperfine interaction with a spin coupling model yields A = -29.6 (2) MHz; this compares well with $A(Fe^{III})$ = -29.5(2) MHz which we obtained here for the Fe^{III} site of the isostructural $Fe^{III}Zn^{II}$ complex.

The study of metal-metal interactions has been an area of fascination for chemists and physicists, because of their potential impact in materials science, catalysis, and metallobiochemistry. The ubiquitous participation of metal sites involving more than one metal center in metalloproteins has heightened the interest of bioinorganic chemists in such interactions. Antiferromagnetic exchange coupling is a prominent feature of the magnetic properties of dicopper sites in hemocyanin, tyrosinase, and laccase[1-3] and diferric sites in plant-type ferredoxins,[4] methemerythrin,[5,6] and ribonucleotide reductase.[7] More recently, double exchange has been used to describe the properties of polyiron centers in ferredoxin II from *Desulfovibrio gigas* and the high potential iron protein.[8] In all these examples the metal-metal interaction represents the dominant factor that determines the spin physics of the metal site, with the zero-field splitting of the individual metal centers (if present) acting as a small perturbation on the spin coupled levels. However, examples of dinuclear sites are emerging wherein the exchange interaction is comparable in magnitude to the zero-field splitting. This is a result of the recent increased focus on the mixed valence and diferrous states of the dinuclear iron-oxo proteins. For example, the dramatic broadening of the EPR signals of the purple acid phosphatase from porcine uterus (uteroferrin) upon phosphate binding is ascribed to such an interplay between antiferromagnetic exchange and zero-field splitting.[9] The integer spin EPR signals observed for the diferrous forms of hemerythrin,[10] ribonucleotide reductase,[11] and methane monooxygenase[12] need to be evaluated in this context as well.

In an effort to understand such systems, we have embarked on combined EPR, Mössbauer, and magnetic susceptibility studies of dinuclear complexes with the goal of describing all the spectroscopic and magnetic properties with a consistent set of parameters. We have taken advantage of our ability to systematically generate heterobimetallic complexes to provide model systems for

[†] University of Minnesota.
[‡] Gray Freshwater Biological Institute.

(1) Solomon, E. I. In *Metal Clusters in Proteins*; Que, L., Jr., Ed.; American Chemical Society: Washington, DC, 1988; pp 116-152.
(2) Solomon, E. I.; Dooley, D. M.; Wang, R. H.; Gray, H. B.; Cerdonio, M.; Mogno, F.; Romani, G. L. *J. Am. Chem. Soc.* **1976**, *98*, 1029-1031.
(3) Petersson, L.; Angstrom, J.; Ehrenberg, A. *Biochim. Biophys. Acta* **1978**, *526*, 311-317.
(4) Sands, R. H.; Dunham, W. R. *Quart. Rev. Biophys.* **1975**, *4*, 443-504.
(5) Dawson, J. W.; Gray, H. B.; Hoenig, H. E.; Rossman, G. R.; Schreder, J. M.; Wang, R. H. *Biochemistry* **1972**, *11*, 461-465.
(6) Maroney, M. J.; Kurtz, D. M., Jr.; Nocek, J. M.; Pearce, L. L.; Que, L., Jr. *J. Am. Chem. Soc.* **1986**, *108*, 6871-6879.
(7) Petersson, L.; Graslund, A.; Ehrenberg, A.; Sjoberg, B.-M.; Reichard, P. *J. Biol. Chem.* **1980**, *255*, 6706-6712.
(8) (a) Papaefthymiou, V.; Girerd, J. J.; Moura, I.; Moura, J. J. G.; Münck, E. *J. Am. Chem. Soc.* **1987**, *109*, 4703-4710. (b) Noodleman, L. *Inorg. Chem.* **1988**, *27*, 3677-3679.
(9) Day, E. P.; David, S. S.; Peterson, J.; Dunham, W. R.; Bonvoisin, J. J.; Sands, R. H.; Que, L., Jr. *J. Biol. Chem.* **1988**, *263*, 15561-15567.
(10) Reem, R. C.; Solomon, E. I. *J. Am. Chem. Soc.* **1987**, *109*, 1216-1226.
(11) Lynch, J. B.; Juarez-Garcia, C.; Münck, E.; Que, L., Jr. *J. Biol. Chem.* **1989**, *264*, 8091-8096.
(12) Fox, B. G.; Surerus, K. K.; Münck, E.; Lipscomb, J. D. *J. Biol. Chem.* **1988**, *263*, 10553-10556.

0002-7863/90/1512-7611$02.50/0

such a study.[13] In this paper we demonstrate this approach with the exchange-coupled half-integer spin system of $[Fe^{III}Ni^{II}BPMP(OPr)_2](BPh_4)_2$. In a forthcoming manuscript we will focus on the integer spin system of $[Fe^{III}Cu^{II}BPMP(Cl)_2](BPh_4)_2$.

We demonstrate here antiferromagnetic exchange coupling for the $Fe^{III}Ni^{II}$ complex. EPR signals have been observed both for the system ground multiplet ($S = 3/2$) and for an excited state ($S = 5/2$) of the spin ladder. Both variable-temperature EPR and magnetic susceptibility studies yield the same value for the exchange coupling parameter J. Mössbauer studies in strong applied fields yield well-resolved spectra for the $S = 3/2$ manifold, from which the zero-field splitting parameters could be determined. Data obtained in weak or moderate magnetic fields reveal strain manifested by a distribution of zero-field splitting parameters around their mean values.

Experimental Section

All reagents and solvents were purchased from commercial sources and used as received unless noted otherwise. Microanalyses were performed by Desert Analytics, Inc., Tucson, AZ. Both 2,6-bis[(bis(2-pyridylmethyl)amino)methyl]-4-methylphenol (HBPMP) and $[Fe^{III}Zn^{II}BPMP(OPr)_2](BPh_4)_2$ were synthesized by published methods.[14,15]

(Bis-μ-*O*,*O'*-propionato)(2,6-bis[(bis(2-pyridylmethyl)amino)-methyl]-4-methylphenolato)iron(III)nickel(II) Bis(tetraphenylborate), $[Fe^{III}Ni^{II}BPMP(OPr)_2](BPh_4)_2 \cdot CH_3COCH_3$. A solution of 0.1 g (0.19 mmol) of HBPMP in 10 mL of methanol was treated with a solution of 0.076 g (0.19 mmol) of HBPMP in 10 mL of methanol was treated with a solution of 0.076 g (0.19 mmol) of $Fe(NO_3)_3 \cdot 9H_2O$ in 5 mL of methanol to yield a dark blue solution, which contains the mononuclear iron complex. Sequential addition of 0.055 g (0.19 mmol) of $Ni(NO_3)_2 \cdot 6H_2O$ in 5 mL of methanol, 0.055 g (0.57 mmol) of sodium propionate in 5 mL of methanol, and a methanolic solution of sodium tetraphenylborate (0.27 g, 0.76 mmol) afforded the crude product, which was filtered through a medium-fritted glass filter. Further purification was achieved by recrystallization of the crude product by vapor diffusion of methanol into an acetone solution of complex. These crystals were of diffraction quality and contained one molecule of occluded acetone. UV-vis (acetone) λ_{max} 385 nm (sh), 570 nm (ϵ = 890 M^{-1} cm^{-1}). Anal. Calcd for $C_{90}H_{89}B_2FeN_6NiO_6$: C, 72.70; H, 6.03; N, 5.65; Fe, 3.76; Ni, 3.95. Found: C, 72.68; H, 6.03; N, 5.58; Fe, 3.93; Ni, 3.83.

Crystallographic Results for $[Fe^{III}Ni^{II}BPMP(OPr)_2](BPh_4)_2 \cdot CH_3COCH_3$. A crystal was mounted on an Enraf-Nonius CAD4 diffractometer. Crystal data, together with details of the diffraction experiment and subsequent calculations, are listed in Table I. The cell dimensions were obtained by least-squares refinement of the setting angles for 25 reflections (2θ = 20–43°). Lorentz and polarization corrections were applied to the data, and absorption corrections based on ψ scans were carried out (correction factors 0.83–1.13).

The structure was solved by using direct methods. Neutral atom scattering factors (including anomalous scattering) were used.[16] All non-H atoms were refined with anisotropic thermal parameters. Hydrogen atoms were included in calculated positions (C–H = 0.95 A, B_H = 3.0). The weighting scheme was based on counting statistics and included a factor (p = 0.05) to downweight the intense reflections. In the final ΔF map, the highest and lowest peaks were 0.67 $e^-Å^{-3}$ and −0.51 $e^-Å^{-3}$, respectively.

The final fractional atomic coordinates for the complex and a complete listing of bond lengths and angles, thermal parameters, and hydrogen atom coordinates are compiled as supplementary material, while selected bond lengths and angles for the complex cation are reported in Table II. The structure of the cation is shown in Figure 1, together with the numbering scheme for the complex.

In view of the apparent disorder in the analogous FeZn structure,[15] the possibility of disorder was tested here. The Fe position was treated as a possible mixture of Fe and Ni as was the Ni position; the occupancy parameter for Fe for one site defines the values for the other three possible metal site occupancies. The positional and thermal parameters at each site were kept the same for both species. Refinement with variable occupancy converged to 66% at the Fe position with R = 0.054, R_w = 0.065, and GOF = 1.51. In light of the correlation between the occupancy and the thermal parameters, the refinement results are suggestive of disorder but not conclusive. Thus, the metal–ligand bonds should not be considered solely due to one metal but rather as having contributions from both. Nevertheless, the disorder does not completely eliminate the uniqueness of the individual metal sites, and it is still possible to distinguish the Fe site from the Ni. The data in Table II represent the metal ion assignments for the predominant occupancy, while the supplementary material includes information for both possible occupancies.

Table I. Crystallographic Experiments and Computations[a] for **1**

formula	$C_{90}H_{89}B_2FeNiN_6O_6$
formula, amu	1486.90
temp, K	297
crystal system	triclinic
space group	$P\bar{1}$
a, Å	13.607 (3)
b, Å	13.700 (3)
c, Å	25.251 (7)
α, deg	77.29 (2)
β, deg	78.25 (2)
γ, deg	61.73 (2)
V, Å^3	4017 (4)
Z	2
D(calc), g cm^{-3}	1.23
crystal dim, mm	0.75 × 0.45 × 0.20
radiation	Mo Kα (λ = 0.7107 Å)
monochromator	graphite
μ, cm^{-1}	4.69
scan type	ω–2θ
2θ range, deg	20.0–43.0
indices collected	$+h,\pm k,\pm l$
reflections	12579
	7077 used ($I > 3.00\sigma(I)$)
no. least sq param	945
data/parameters	7.49
R^{*b}	0.054
$R_w{}^b$	0.065
GOF^b	1.48
p[a]	0.05

[a] All calculations were performed by using Texsan-Texray Structure Analysis Package, Molecular Structure Corporation, 1985. The intensity data were processed as described in *CAD 4* and *SDP-PLUS User's Manual*; B. A. Frenz & Assoc.; College Station, TX, 1982. The net intensity $I = [K(NPI)](C - 2B)$, where K = 17.50 (attenuator factor), NPI = ratio of fastest possible scan rate to scan rate for the measurement, C = total count, and B = total background count. The standard deviation in the net intensity is given by $[\sigma(I)]^2 = (k/NPI)^2[C + 4B + (pI)^2]$ where p is a factor used to downweight intense reflections. The observed structure factor amplitude F_o is given by $F_o = (I/Lp)^{1/2}$, where Lp = Lorentz and polarization factors. The $\sigma(I)$'s were converted to the estimated errors in the relative structure factors $\sigma(F_o)$ by $\sigma(F_o) = {}^1/_2[\sigma(I)/I]F_o$. [b] $R = (\sum||F_o| - |F_c||)/(\sum|F_o|)$; $R_w = \{(\sum w|F_o| - |F_c|^2)/\sum w(F_o)^2)\}^{1/2}$; GOF = $\{(\sum w(||F_o| - |F_c||)^2)/(N_{data} - N_{params})\}^{1/2}$.

Physical Methods. X band EPR measurements were performed on a Varian E9 spectrometer by using a liquid helium flow cryostat (Oxford). Spectra were digitally recorded, and the data were analyzed by using an IBM-PC compatible computer. The spectra reported here and those used for the temperature dependence study were recorded in the nonsaturating microwave power regime.

The sample temperature was determined by immersing a calibrated, carbon-glass resistance sensor (Lakeshore, CGR-1-1000) in the sample at a position immediately above the cavity (the Q was not significantly lowered). A four-point measurement was made through no. 34 manganine wires which were attached to short leads of the sensor. The top of the sample tube was sealed with wax to prevent the accumulation of liquid air which may conduct heat from the top of the EPR tube and thereby increase the temperature gradient at the sample. To further minimize temperature gradients, the length of the sample was kept small (2 cm), and the bottom of the EPR tube did not rest on the sample support since this constricts helium flow.

Magnetic measurements were carried out with a Quantum Design SQUID magnetometer at an applied field of 0.3 T. Samples typically weighed 50 mg. The independence of the susceptibility against the magnetic field was checked at room temperature. Mercuric tetrakis(thiocyanato)cobaltate was used as a susceptibility standard. The un-

(13) (a) Borovik, A. S.; Que, L., Jr.; Papaefthymiou, V.; Münck, E.; Taylor, L. F.; Anderson, O. P. *J. Am. Chem. Soc.* **1988**, *110*, 1986–1988. (b) Suzuki, M.; Uehara, A.; Oshio, H.; Endo, K.; Yanaga, M.; Kida, S.; Saito, K. *Bull. Chem. Soc. Jpn.* **1987**, *60*, 3547–3555.

(14) Suzuki, M.; Kanatomi, H.; Murase, I. *Chem. Lett., Chem. Soc. Jpn.* **1981**, 1745–1748.

(15) Borovik, A. S.; Papaefthymiou, V.; Taylor, L. F.; Anderson, O. P.; Que, L., Jr. *J. Am. Chem. Soc.* **1989**, *111*, 6183–6195.

(16) *International Tables for X-ray Crystallography*; Kynoch Press: Birmingham, England, 1969; Vol. IV, pp 55, 99, 149.

Table II. Selected Bond Lengths (Å) and Angles (deg) for **1**[a]

a. Bond Lengths

Ni-O1	2.004 (4)	C12-C13	1.385 (9)	N3-C19	1.347 (7)
Ni-O2	1.978 (4)	C15-C16	1.373 (8)	N5-C22	1.344 (7)
Ni-O3	2.050 (4)	C17-C18	1.363 (9)	N5-C26	1.343 (7)
Ni-N1	2.114 (5)	C21-C26	1.507 (8)	N6-C28	1.342 (7)
Ni-N2	2.108 (5)	C23-C24	1.38 (1)	C1-C2	1.396 (7)
Ni-N3	2.076 (4)	C25-C26	1.366 (8)	C3-C4	1.402 (9)
O1-C1	1.371 (6)	C28-C29	1.366 (8)	C4-C5	1.380 (8)
O3-C35	1.237 (7)	C30-C31	1.38 (1)	C4-C37	1.530 (9)
O5-C33	1.263 (7)	C33-C34	1.503 (8)	C6-C20	1.498 (8)
N1-C8	1.491 (7)	C34-C39	1.46 (1)	C9-C10	1.397 (8)
N2-C9	1.343 (7)	Fe-Ni	3.378 (8)	C11-C12	1.38 (1)
N3-C15	1.338 (7)	Fe-O1	1.975 (3)	C14-C15	1.497 (8)
N4-C20	1.495 (6)	Fe-O4	1.958 (4)	C16-C17	1.376 (9)
N4-C21	1.488 (7)	Fe-O5	2.009 (4)	C18-C19	1.378 (8)
N4-C27	1.479 (7)	Fe-N4	2.141 (4)	C22-C23	1.371 (8)
N6-C32	1.340 (7)	Fe-N5	2.119 (5)	C24-C25	1.374 (9)
C1-C6	1.385 (8)	Fe-N6	2.086 (4)	C27-C28	1.500 (8)
C2-C3	1.392 (8)	O2-C33	1.265 (7)	C29-C30	1.379 (9)
C2-C7	1.489 (8)	O4-C35	1.281 (7)	C31-C32	1.372 (8)
C5-C6	1.399 (8)	N1-C7	1.484 (7)	C35-C36	1.505 (9)
C8-C9	1.494 (8)	N1-C14	1.485 (7)	C36-C38	1.33 (1)
C10-C11	1.371 (9)	N2-C13	1.338 (7)		

b. Bond Angles (deg)

O1-Ni-O2	98.6 (2)	O1-Fe-O4	99.1 (2)
O1-Ni-O3	90.3 (2)	O1-Fe-O5	91.0 (2)
O1-Ni-N1	90.0 (2)	O1-Fe-N4	89.9 (2)
O1-Ni-N2	87.1 (2)	O1-Fe-N5	86.4 (2)
O1-Ni-N3	167.3 (2)	O1-Fe-N6	165.9 (2)
O2-Ni-O3	92.5 (2)	O4-Fe-O5	93.2 (2)
O2-Ni-N1	169.3 (2)	O4-Fe-N4	167.8 (2)
O2-Ni-N2	93.3 (2)	O4-Fe-N5	92.7 (2)
O2-Ni-N3	93.5 (2)	O4-Fe-N6	94.8 (2)
O3-Ni-N1	93.9 (2)	O5-Fe-N4	95.0 (2)
O3-Ni-N2	174.0 (2)	O5-Fe-N5	173.9 (2)
O3-Ni-N3	85.4 (2)	O5-Fe-N6	85.6 (2)
N1-Ni-N2	80.7 (2)	N4-Fe-N5	79.4 (2)
N1-Ni-N3	78.4 (2)	N4-Fe-N6	76.8 (2)
N2-Ni-N3	96.0 (2)	N5-Fe-N6	95.6 (2)
Ni-O1-C1	121.2 (3)	Fe-O1-C1	122.5 (3)
Ni-O2-C33	130.9 (4)	Fe-O4-C35	131.2 (4)
Ni-O3-C35	134.0 (4)	Fe-O5-C33	133.7 (4)
Ni-N1-C7	112.5 (3)	Fe-N4-C20	111.6 (3)
Ni-N1-C8	108.8 (3)	Fe-N4-C21	109.3 (3)
Ni-N1-C14	104.2 (3)	Fe-N4-C27	105.0 (3)
Ni-N2-C9	113.7 (4)	Fe-N5-C22	124.3 (4)
Ni-N2-C13	124.8 (2)	Fe-N5-C26	115.4 (4)
Ni-N3-C15	114.3 (4)	Fe-N6-C28	114.9 (4)
Ni-N3-C19	127.4 (4)	Fe-N6-C32	126.5 (4)
Ni-O1-Fe	116.2 (2)		

[a] Estimated standard deviations in the least significant digits are given in parentheses.

certainty of the temperature was about 0.1 K and that of the susceptibility about 115 × 10^{-6} cm^3 mol^{-1}. It follows that the uncertainty of $\chi_m T$ is about 0.035 cm^3 mol^{-1} K. The number of measured points was around 60. The diamagnetism corrected for Pascals constants of the ligand was estimated as −840 × 10^{-6} cm^3 mol^{-1}. The holder used in the experiment was a suspended geltain capsule; its paramagnetism was negligible.

The Mössbauer experiments were performed in a Janis dewar which housed a 6.0 T superconducting magnet. Throughout the experiments the ^{57}Co(Rh) source was kept at 4.2 K. Isomer shifts are quoted relative to Fe metal at 300 K.

Results and Discussion

Description of Solid-State Structure. [$Fe^{III}Ni^{II}$BPMP-$(OPr)_2$]$(BPh_4)_2$·CH_3COCH_3. The structure of the compound (Figure 1) shows an iron and a nickel atom bridged by the phenolate oxygen atom of BPMP and by two additional propionate ligands to form a triply bridged dinuclear core. Structurally characterized complexes with such a core structure now include Fe^{III}_2,[17-20] $Fe^{II}Fe^{III}$,[13,15,21] Fe^{II}_2,[22-24] $Mn^{II}Mn^{III}$,[25-28] Ni^{II}_2,[29] and

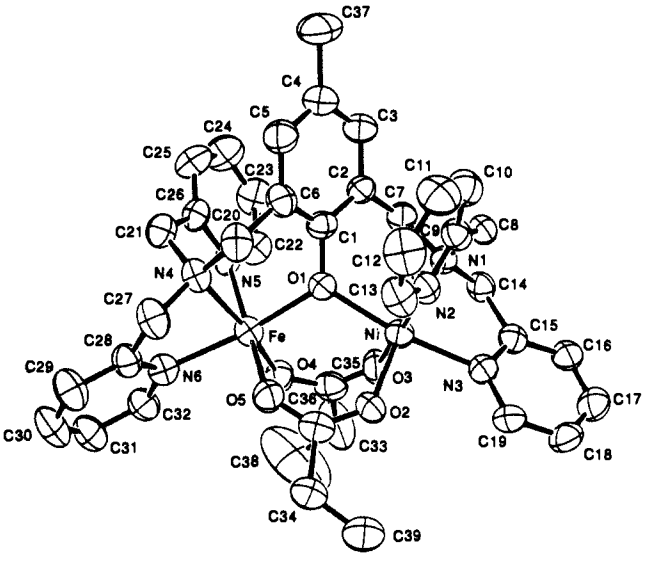

Figure 1. ORTEP plot of the structure of $[Fe^{III}Ni^{II}BPMP(OPr)_2]^{2+}$ showing 50% probability ellipsoids.

$Fe^{III}Zn^{II}$[13,15] complexes. In general, the $Fe^{III}Ni^{II}$ complex shares many of the structural properties of the related complexes, since the properties are most likely imposed by the requirements of the dinucleating ligand. The phenolate ring plane is rotated relative to the Fe–O–Ni plane, the N(amine)–M–N(pyridine) angles are significantly less than 90°, and the shorter M–O(carboxylate) bonds are trans to the tertiary amine nitrogen atoms. The Fe–Ni separation, 3.38 Å, is comparable to the values found in other complexes.

A comparison of the metric parameters of the individual six-coordinate metal centers relative to those found in similar complexes in this series shows values expected for the relative ionic radii of the different metal ions and the metal disorder found in the heterobimetallic complexes. Thus for the $Fe^{III}Ni^{II}$ and $Fe^{III}Zn^{II}$ complexes the average M^{II}–O and M^{II}–N values differ only by the difference in the atomic radii (0.840 Å for Ni^{II} and 0.885 Å for Zn^{II}).[30] The average Ni^{II}–O and Ni^{II}–N values are 2.01 and 2.10 Å, respectively; the corresponding values for the $Fe^{III}Zn^{II}$ complex are 2.05 and 2.14 Å, respectively. $[Ni^{II}_2$(BIMP)-$(OAc)_2](ClO_4)$[29a] where BIMP = 2,6-bis[(bis(1-methyl-2-imidazole)amino)methyl]-4-methylphenol also has longer M^{II}–O

(17) (a) Armstrong, W. H.; Spool, A.; Papaefthymiou, G. C.; Frankel, R. B.; Lippard, S. J. *J. Am. Chem. Soc.* **1984**, *106*, 3653-3667. (b) Wieghardt, K.; Pohl, K.; Gebert, W. *Angew. Chem., Int. Ed. Engl.* **1983**, *22*, 727-728. (c) Spool, A.; Williams, I. D.; Lippard, S. J. *Inorg. Chem.* **1985**, *24*, 2156-2162.

(18) Armstrong, W. H.; Lippard, S. J. *J. Am. Chem. Soc.* **1984**, *106*, 4632-4633.

(19) Murch, B. P. Ph.D. Thesis, Cornell University, 1987.

(20) Murch, B. P.; Bradley, F. C.; Que, L., Jr. *J. Am. Chem. Soc.* **1986**, *108*, 5027-5028.

(21) Mashuta, M. S.; Webb, R. J.; Oberhausen, K. J.; Richardson, J. F.; Buchanan, R. M.; Hendrickson, D. N. *J. Am. Chem. Soc.* **1989**, *111*, 2745-2746.

(22) (a) Chaudhuri, P.; Wieghardt, K.; Nuber, B.; Weiss, J. *Angew. Chem., Int. Ed. Engl.* **1985**, *24*, 778-779. (b) Hartman, J. R.; Rardin, R. L.; Chaudhuri, P.; Pohl, K.; Wieghardt, K.; Nuber, B.; Weiss, J.; Papaefthymiou, G. C.; Frankel, R. B.; Lippard, S. J. *J. Am. Chem. Soc.* **1987**, *109*, 7387-7396.

(23) Tolman, W. B.; Bino, A.; Lippard, S. J. *J. Am. Chem. Soc.* **1989**, *111*, 8522-8523.

(24) Borovik, A. S.; Que, L., Jr. *J. Am. Chem. Soc.* **1988**, *110*, 2345-2347.

(25) Suzuki, M.; Mikuriya, M.; Murata, S.; Uehara, A.; Oshio, H.; Kida, S.; Saito, K. *Bull. Chem. Soc. Jpn.* **1987**, *60*, 4305-4312.

(26) (a) Diril, H.; Chang, H.-R.; Zhang, X.; Larsen, S. R.; Potenza, J. A.; Pierpont, C. G.; Schugar, H. J.; Isied, S. S.; Hendrickson, D. N. *J. Am. Chem. Soc.* **1987**, *109*, 6207-6208. (b) Diril, H.; Chang, H.-R.; Nilges, M. J.; Zhang, X.; Potenza, J. A.; Schugar, H. J.; *Isied*, S. S.; Hendrickson, D. N. *J. Am. Chem. Soc.* **1989**, *111*, 5102-5114.

(27) Buchanan, R. M.; Oberhausen, K. J.; Richardson, J. F. *Inorg. Chem.* **1988**, *27*, 971-973.

(28) Bashkin, J. S.; Schake, A. R.; Vincent, J. B.; Chang, H.-R.; Li, Q.; Huffman, J. C.; Christou, G.; Hendrickson, D. N. *J. Chem. Soc., Chem. Commun.* **1988**, 700-702.

(29) (a) Buchanan, R. M.; Mashuta, M. S.; Oberhausen, K. J.; Richardson, J. F.; Li, Q.; Hendrickson, D. N. *J. Am. Chem. Soc.* **1989**, *111*, 4497-4498. (b) Chaudhuri, P.; Küppers, H.-J.; Wieghardt, K.; Gehring, S.; Haase, W.; Nuber, B.; Weiss, J. *J. Chem. Soc., Dalton Trans.* **1988**, 1367-1370.

(30) Shannon, R. D.; Prewitt, C. T. *Acta Crystallogr.* **1969**, *B25*, 925-946.

(2.04 Å) and M^{II}–N (2.12 Å) values relative to the $Fe^{III}Ni^{II}$ BPMP complex, undoubtedly attributed to the shorter Fe^{III}–L components averaged into the Ni^{II}–L values.

EPR, Magnetic Susceptibility, and Mössbauer Studies. Before presenting the data, we wish to assemble the spin Hamiltonian appropriate for describing the magnetic data. The complex to be described consists of an exchange-coupled pair of Fe^{III} (S_1 = 5/2) and Ni^{II} (S_2 = 1) ions. A suitable spin Hamiltonian for describing the low-lying electronic states can be written as

$$\mathcal{H} = J\mathbf{S}_1\cdot\mathbf{S}_2 + \sum_{i=1}^{2}[\mathbf{S}_i\cdot\mathbf{D}_i\cdot\mathbf{S}_i + \beta\mathbf{S}_i\cdot\mathbf{g}_i\cdot\mathbf{H}] \quad (1)$$

where J is the exchange coupling parameter. The tensors $\mathbf{D}_i$ describe the zero-field splittings of the two ions. In its principal axis form this interaction is usually written as

$$\mathcal{H}_{ZF} = D_i\left[S_{iz}^2 - \tfrac{1}{3}S_i(S_i+1) + \frac{E_i}{D_i}(S_{ix}^2 - S_{iy}^2)\right] \quad (2)$$

The Zeeman interaction of the high-spin ferric ion is isotropic, g_1 = 2.0. If the exchange interaction dominates, it is useful to work in a coupled representation, replacing the local spins $\mathbf{S}_i$ by the system spin $\mathbf{S}$, $\mathbf{S} = \mathbf{S}_1 + \mathbf{S}_2$. The coupling yields three multiplets with S = 3/2, 5/2, and 7/2 at energies

$$E(S) = J[S(S+1) - 4\tfrac{3}{4}]/2 \quad (3)$$

The electronic properties of each multiplet can be described by

$$\mathcal{H}_e = D\left[S_z^2 - \tfrac{1}{3}S(S+1) + \frac{E}{D}(S_x^2 - S_y^2)\right] + \beta\mathbf{S}\cdot\mathbf{g}\cdot\mathbf{H} \quad (4)$$

where D, E, and $\mathbf{g}$ now refer to the system. By using the expressions given by Scaringe et al.,[31] we express the parameters of eq 4 by those of the uncoupled sites, obtaining for the S = 3/2 multiplet

$$\mathbf{g} = \tfrac{7}{5}\mathbf{g}_1 - \tfrac{2}{5}\mathbf{g}_2 \quad (5)$$

$$\mathbf{D} = \tfrac{28}{15}\mathbf{D}_1 + \tfrac{1}{15}\mathbf{D}_2 \quad (6)$$

Figure 2 depicts schematically the multiplets for antiferromagnetic coupling, $J > 0$, and $J \gg |D|$.

With Mössbauer spectroscopy we focus on the hyperfine interactions of the Fe^{III} site. For the analysis of the low-temperature spectra we amend eq 4 with terms describing the magnetic hyperfine, the electric quadrupole, and the nuclear Zeeman interactions, respectively,

$$\mathcal{H}_{hf} = A\mathbf{S}\cdot\mathbf{I} + \frac{eQV_{zz}}{12}[3I_z^2 - 15/4 + \eta(I_x^2 - \mathbf{I}_y^2)] - g_n\beta_n\mathbf{H}\cdot\mathbf{I} \quad (7)$$

where I is the spin operator of the ^{57}Fe nucleus. The magnetic hyperfine coupling constant, A, is defined in the coupled system; it is related to that of the local site by

$$A = \tfrac{7}{5}A_1 \quad (8)$$

for S = 3/2. In the presence of an external magnetic field the magnetic hyperfine term of eq 7 can be written as $-g_n\beta_n\mathbf{H}_{int}\cdot\mathbf{I}$, where the internal field, $\mathbf{H}_{int}$, is given by

$$\mathbf{H}_{int} = -A\langle\mathbf{S}\rangle/g_n\beta_n \quad (9)$$

The data reported here are in the slow relaxation limit; thus, four distinct Mössbauer spectra are observed from the S = 3/2 quartet, one for each sublevel of the multiplet. The expectation value of the electronic spin, $\langle\mathbf{S}\rangle$, can be computed for each level by diagonalization of

$$\mathcal{H} = \mathcal{H}_e + \mathcal{H}_{hf} \quad (10)$$

EPR Studies. X-band EPR spectra of an acetonitrile solution of the $Fe^{III}Ni^{II}$ complex are shown in Figure 3. The solution is magnetically dilute as the shape of the spectra is independent of concentration in the range 0.1–7 mM complex. EPR spectra of powder samples show features which are similar to the solution

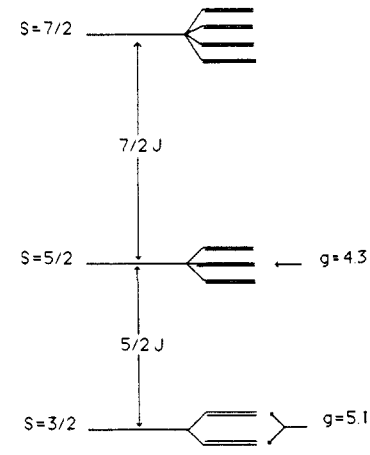

Figure 2. Spin ladder, including zero-field splittings, appropriate for $[Fe^{III}Ni^{II}BPMP(OPr)_2](BPh_4)_2$. Arrows indicate the doublets from which the major observed EPR resonances originate.

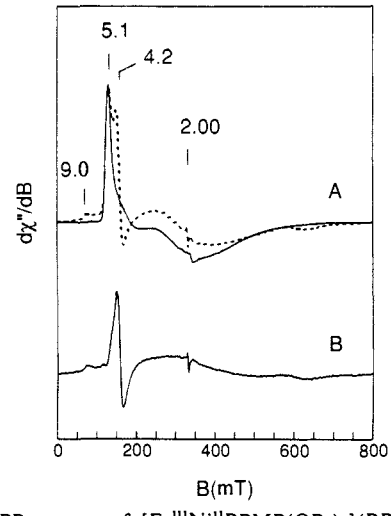

Figure 3. EPR spectra of $[Fe^{III}Ni^{II}BPMP(OPr)_2](BPh_4)_2$ in frozen CH_3CN solution, recorded at 2.6 K (solid line in (A)) and 44 K (dashed). Population of the excited S = 5/2 multiplet at 44 K is evident by the appearance of signals at g = 4.2 and $g \simeq 9$. The S = 5/2 signals shown in (B) were obtained by subtracting the 2.6 K spectrum from that obtained at 44 K. In order to facilitate comparison, the amplitude of the 44 K spectrum in (A) was increased by the factor 19. Instrumental parameters: microwave frequency, 9.23 GHz at 0.2 mW; modulation amplitude, 2 mT; dB/dt, 3.3 mT/s. The small derivative-shaped signal at g = 2 is an impurity.

spectra; the differences are presumably due to intermolecular magnetic interactions. The T = 2.6 K solution spectrum (solid line) of Figure 3A exhibits a prominent resonance at g = 5.1 and broad features in the range $3 > g > 1$. Figure 4 shows the temperature dependence of the g = 5.1 feature (signal times T versus T). Note that $T[d\chi''/dB]$ is essentially constant for $T <$ 6 K. The observed EPR spectrum can be interpreted with an S = 3/2 spin Hamiltonian.

For $\beta H \ll |D|$, eq 4 produces two Kramers doublets, the Zeeman splitting of which can be described by effective g values. For $g_x = g_y = g_z$ = 2.00 in eq 4, the effective g values of each doublet depend only on E/D. A plot of effective g values, g' versus E/D is shown in Figure 5. The Mössbauer spectra discussed below show that $D \approx 0.7$ cm^{-1} and that E/D is centered around E/D = 0.32; for this value of E/D both doublets have essentially the same g values and thus contribute very similar spectra. This explains the observed zero slope at low temperature when $[d\chi''/dB]$ is plotted versus T.

The type of EPR spectrum observed here is similar to published spectra of other S = 3/2 systems, e.g., Fe_4S_4 clusters.[32] The line

(31) Scaringe, R. P.; Hodgson, D. J.; Hatfield, W. E. *Mol. Phys.* **1978**, *35*, 701–713.

(32) Carney, M. J.; Papaefthymiou, G. C.; Spartalian, K.; Frankel, R. B.; Holm, R. H. *J. Am. Chem. Soc.* **1988**, *110*, 6084–6094.

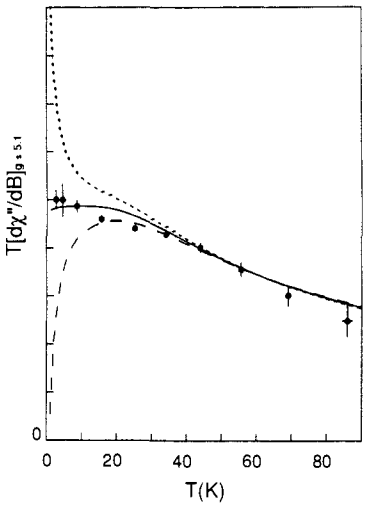

Figure 4. Temperature dependence of the $g = 5.1$ signal. The signal intensity was determined by measuring the zero-to-peak height, after subtraction of the excited $S = 5/2$ resonance. For $T > 50$ K relaxation causes line broadening which yields inaccurate, low readings of the intensity. The theoretical curves are based on eqs 3 and 4 by using $J = 24$ cm^{-1}, $D = 0.7$ cm^{-1}, $E/D = 0.32$. The short and long dashed curves give the contributions of the ground and excited doublets of the $S = 3/2$ multiplet, respectively; the solid curve is the sum of the two doublet contributions.

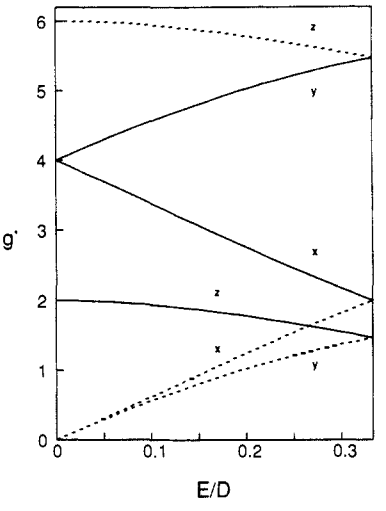

Figure 5. Effective g values for the two Kramers doublets of an $S = 3/2$ doublet according to eq 4 for $g_x = g_y = g_z = 2.00$.

shapes of these spectra are dominated by a distribution of E/D. Figure 6A (solid) shows a simulated $T = 2.6$ K spectrum, by using the Mössbauer parameters and the contributions of both doublets and $\sigma_{E/D} = 0$. The simulation is much sharper than the data. However, a simple Gaussian distribution of E/D centered at 0.32 of width $\sigma_{E/D} = 0.1$ (1 standard deviation) describes the essential features of the data (Figure 6A, dashed) remarkably well. Unrelated to the effects of the distribution in E/D, the position of the low field resonance in the simulated spectra is at a significantly lower field than that of the data. The simulation of Figure 6B, overlaid on the data, results from adjustments of the theoretical g value to 5.1 (see Conclusions).

The spread in E/D results in a spread of g values given by

$$\Delta g_i = [\mathrm{d}g/\mathrm{d}(E/D)]_{i,E/D}\Delta(E/D), \qquad i = x,y,z \qquad (11)$$

and is typically referred to as g strain.[33] The quantities $[\mathrm{d}g/\mathrm{d}(E/D)]_i$ at $E/D = 0.32$ can be obtained from Figure 5. They vary by about a factor of 2, which is rather small when compared to a $S = 5/2$ complex at $E/D = 0$ where the variation is approximately a factor of 70. The dominant broadening effects are

(33) Hagen, W. R.; Hearshen, D. O.; Sands, R. H.; Dunham, W. R. *J. Magn. Reson.* **1985**, *61*, 220–232.

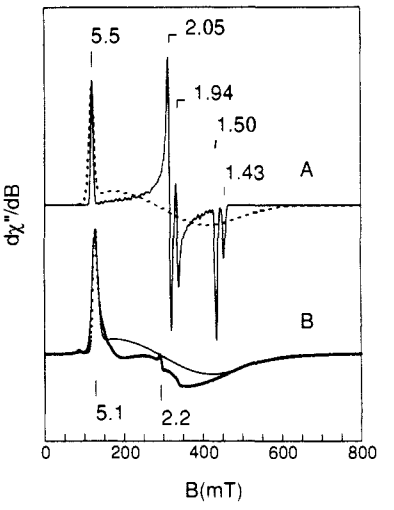

Figure 6. Spectral simulations of the $S = 3/2$ EPR spectrum. The solid line in (A) shows a theoretical spectrum generated from eq 4 for $T = 2.6$ K, $D = 0.7$ cm^{-1}, $E/D = 0.32$, and $g_x = g_y = g_z = 2.00$, by using an intrinsic line width of 3 mT. The dashed line in (A) results when E/D is distributed with $\sigma_{E/D} = 0.1$ according to the Mössbauer analysis of Figure 11A. The assumption of $\mathbf{g} = 2.00$ places the low-field resonances at $g' = 5.5$ rather than at $g' = 5.1$ as observed experimentally (point-trace in (B)). Adjusting g_y and g_z to 1.86 produced a correct fit. Since the g values of Fe^{III} sites are close to $g_1 = 2.00$, lowering the values of g_x and g_y can be attributed, according to eq 5, to the g tensor of the Ni^{II} site.

realized when this g strain is converted into "B-strain" with the relation

$$\Delta B = -\frac{h\nu}{\beta}\frac{\Delta g}{g^2} \qquad (12)$$

Thus, the largest and smallest g values of the $S = 3/2$ spectrum have field widths that differ by an order of magnitude, rationalizing why the high field features of the spectrum of Figure 6B are so broad.

Upon increasing the temperature, a new resonance appears around $g = 4.2$. Its intensity increases steadily up to $T \simeq 90$ K; at temperatures above 50 K all signals broaden due to fast relaxation. A characteristic spectrum, recorded at 44 K, is shown in Figure 3A (dashed). We have subtracted the 2.6 K spectrum from the 44 K spectrum in such a way that removal of the $g = 5.1$ resonance generates a reasonable baseline in that spectral region. The difference spectrum shown in Figure 3B is reminiscent of those observed for $S = 5/2$ states with $E/D \simeq 1/3$. A closer inspection of the data taken at a higher gain reveals a weak resonance around $g \simeq 9.5$, as expected for an $S = 5/2$ system. This indicates that the $g = 4.2$ resonance belongs to the middle Kramers doublet of the excited $S = 5/2$ manifold of the spin ladder of Figure 2. We have produced similar difference spectra for the temperature range from 10 to 85 K; in Figure 7 the area of the integrated $g = 4.2$ resonance times T is plotted versus T. A fit to the energy levels predicted by eq 3 yielded $J = 24$ cm^{-1}.[34] As shown in Figure 4 the value $J = 24$ cm^{-1} also accounts for the temperature dependence of the $g = 5.1$ resonance. While the zero-field splittings are too small to affect the temperature dependence of the $S = 5/2$ resonance, a zero-field splitting of $D \simeq 0.7$ cm^{-1} for the $S = 3/2$ multiplet is required to account for the behavior of the $g = 5.1$ resonance below $T \simeq 6$ K.

Magnetic Susceptibility Studies. We have measured the susceptibility of the $Fe^{III}Ni^{II}$ complex as polycrystalline material as well as in acetonitrile solution by using a SQUID magnetometer. The results were the same. Figure 8 shows a plot of χT vs T for the polycrystalline material. The solid line is a theoretical curve, generated by diagonalization of eq 1 for $J = +23$ cm^{-1}. This value is in agreement with that obtained by EPR. The zero-field splitting

(34) Because of relaxation broadening, the $T = 85$ K data point is perhaps the least reliable. If this point is excluded from the analysis, a significantly better fit is obtained, yielding $J = +28$ cm^{-1}.

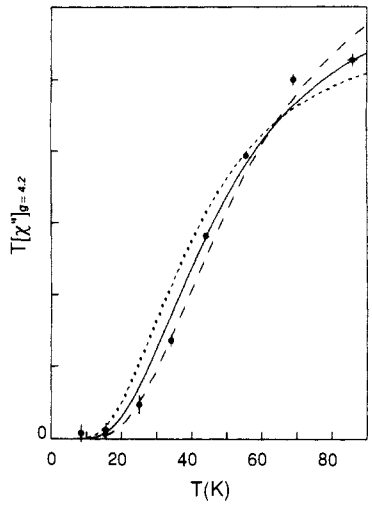

Figure 7. Temperature dependence of the $g = 4.2$ resonance (solid circles) of the $S = 5/2$ multiplet. After subtraction of the $S = 3/2$ signals, the signal intensity was taken as peak-to-peak amplitude times peak-to-peak width. Like the $g = 5.1$ resonance, the $g = 4.2$ signal broadens above 50 K; the effect of broadening is partly accounted for by using amplitude times width as the measure. The solid line is a theoretical curve computed by use of eq 3 with $J = 24$ cm^{-1}. The dashed lines result from choosing $J = 20$ (short dash) and $J = 28$ cm^{-1} (long dash).

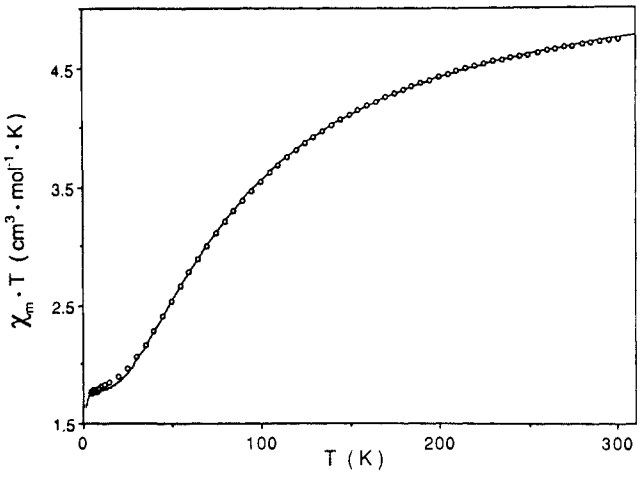

Figure 8. Experimental (···) and theoretical (—) temperature dependences of $\chi_m T$ for the polycrystalline sample of $[Fe^{III}Ni^{II}BPMP(OPr)_2](BPh_4)_2$. The theoretical curve was generated from eq 1 by using $J = 23$ cm^{-1}, $D_1 = 0.4$ cm^{-1}, $(E_1/D_1) = 0.32$, $g_{1x} = g_{1y} = g_{1z} = 2.0$ for Fe^{III}; and $D_2 = 0$, $g_{2x} = g_{2y} = g_{2z} = g_{av} = 2.1$ for Ni^{II}. We also applied a 600×10^{-6} cm^3 mol^{-1} correction for temperature-independent paramagnetism (TIP).

parameters are important only at temperatures below 10 K; we have therefore made the following simplifying assumptions. Equation 6 suggests that the D value of the Ni^{II} may contribute little to the zero-field splitting of the multiplet; thus, we have set $D_2 = 0$. We have fixed E/D of the Fe^{III} site to 0.32, by using the EPR information. Finally, we have set $g_1 = 2.0$ and replaced the unknown g values of the Ni^{II} by an average g value, g_{av}. The best simulation was obtained for $D_1 = 0.41$ cm^{-1}, corresponding to $D = 0.76$ cm^{-1} and $g_{av} = 2.10$. The D value agrees well with the D values obtained by EPR and Mössbauer spectroscopy.

Mössbauer Studies. We have studied the Mössbauer spectra of ^{57}Fe enriched samples of $Fe^{III}Ni^{II}$ complex in frozen acetonitrile solutions in the temperature range from 1.4 to 160 K and applied magnetic fields up to 6.0 T. Some representative spectra are shown in Figures 9, 10, and 11. The solid lines drawn through the spectra are the results of spectral simulations by using the Hamiltonian of eqs 4, 7, and 10, with the parameters listed in Table III. We comment on the essential features of the spectra in the following.

We obtained the isomer shift, $\delta = 0.46$ (3) mm/s, from the center of gravity of the spectra. From the observation of para-

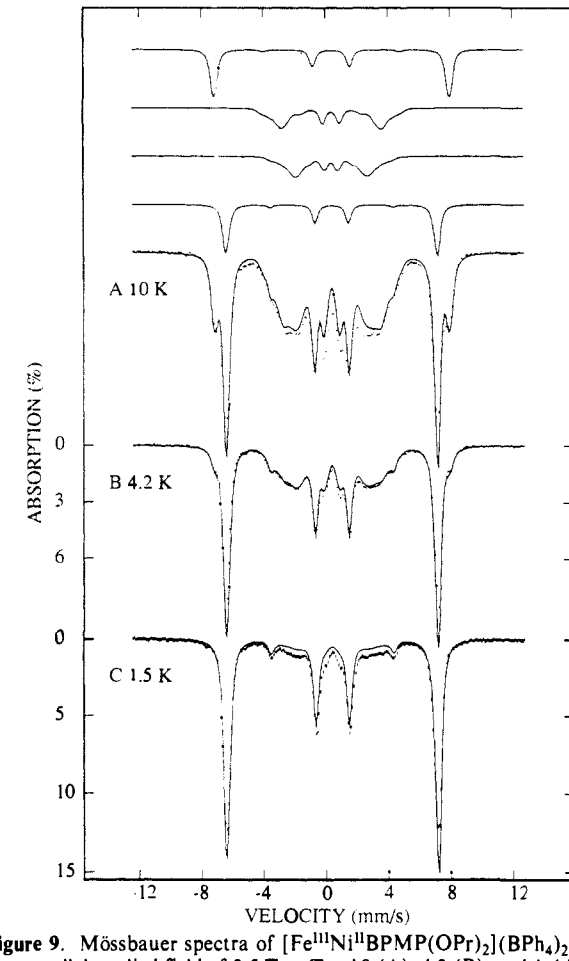

Figure 9. Mössbauer spectra of $[Fe^{III}Ni^{II}BPMP(OPr)_2](BPh_4)_2$ taken in a parallel applied field of 2.5 T at $T = 10$ (A), 4.2 (B), and 1.4 K (C). The solid lines are theoretical curves generated from diagonalization and powder averaging of eq 10, by using the parameters listed in Table III. The spectra are superpositions of four subcomponents, each associated with a particular level of the $S = 3/2$ multiplet. The four individual spectra are indicated above the data.

magnetic hyperfine structure in weak applied fields and in accord with the EPR results, we conclude that the electronic spin relaxes slowly on the Mössbauer time scale (10^{-7} s) for $T < 10$ K. The magnetic hyperfine coupling constant, A, is most reliably determined from the 6.0 T spectrum taken at 1.4 K (Figure 10B). At 6.0 T the electronic Zeeman term dominates, and the $M_S = -3/2$ state is the only level appreciably populated. Moreover, under these conditions, the components of $\langle \mathbf{S} \rangle$, $\langle S_j \rangle \simeq -3/2$, are practically independent of D and E and are thus little affected by a distribution in these parameters. From the value $A = -41.4$ MHz and relation (8) we obtain $A_1 = -29.5$ (2) MHz. This compares very well with $A(Fe^{III}) = -29.6$ (2) MHz of the high-spin ferric site of the corresponding $Fe^{III}Zn^{II}$ complex (see below). Thus, the values for A_1 and δ show clearly that the ferric site of the $Fe^{III}Ni^{II}$ complex is high-spin ($S_1 = 5/2$). Because the local spin of the iron site has $S_1 = 5/2$ and the system ground state has $S = 3/2$, it follows that the Ni^{II} is high-spin, $S_2 = 1$, as expected for octahedral Ni^{II} and stated without proof in the introductory part of this section.

In magnetic fields of intermediate strength we observed Mössbauer spectra consisting of a superposition of four spectral components, one from each of the four substates of the $S = 3/2$ manifold. As an example, 2.5 T spectra and their deconvolution are shown in Figure 9. The splittings and populations of the individual components depend on the parameters D and E. While $\langle \mathbf{S} \rangle$ of the individual levels depends on D and E, this quantity is practically independent of $\mathbf{g}$. (We will comment on this point further below.)

As pointed out above, the line shapes of the $S = 3/2$ EPR spectra reflect extensive strain. The presence of strain is also

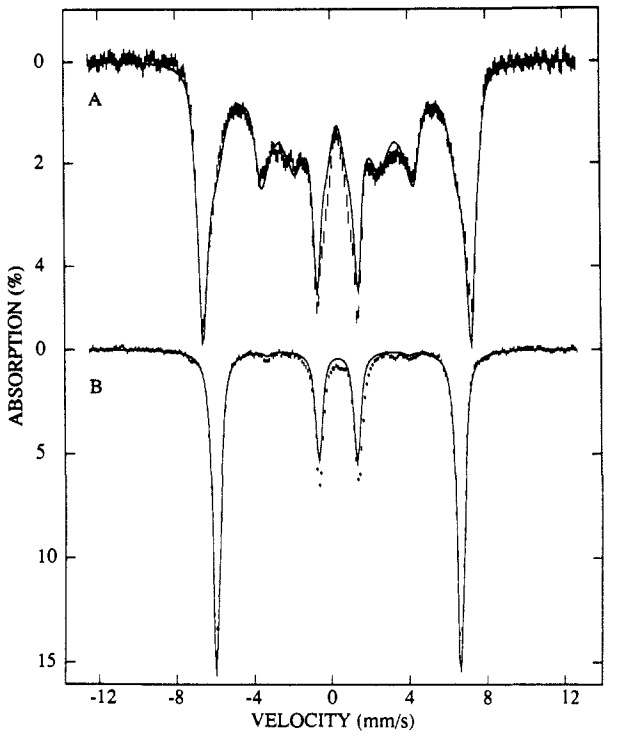

Figure 10. Mössbauer spectra of $[Fe^{III}Ni^{II}BPMP(OPr)_2](BPh_4)_2$ in frozen acetonitrile soution: (A) T = 4.2 K and 1.0 T parallel field and (B) T = 1.4 K and 6.0 T parallel field. The solid lines are theoretical curves computed with the parameters of Table III.

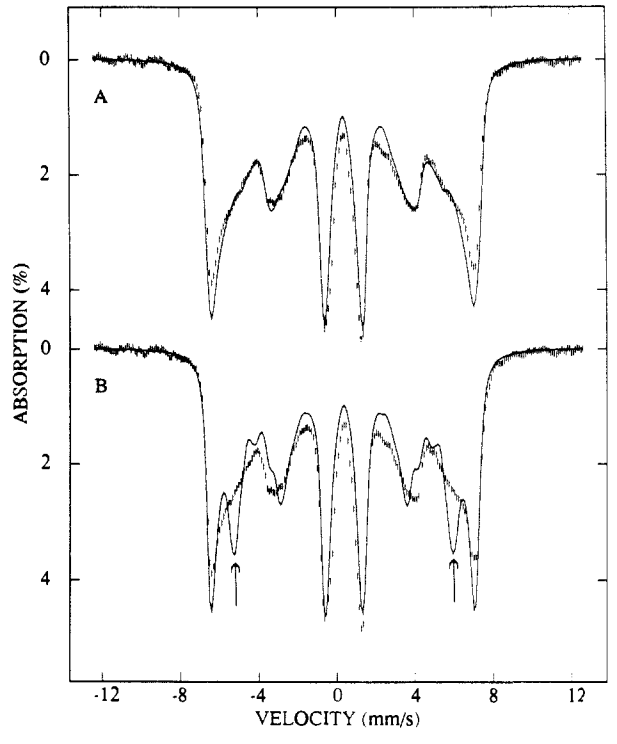

Figure 11. Mössbauer spectrum of $[Fe^{III}Ni^{II}BPMP(OPr)_2](BPh_4)_2$ recorded at 1.4 K in a 0.4 T parallel field. The solid line in (B) is a theoretical curve computed with the parameters of Table III. The curve in (A) was computed from the same parameter set, except that E/D was assumed to be distributed about its mean, E/D = 0.32, with $\sigma_{E/D}$ = 0.10.

evident in the low field Mössbauer spectra. Figure 11A,B shows a 1.4-K spectrum recorded in a 0.4-T parallel applied field. The solid line in Figure 11B is a simulation using the parameter set of Table III. It is evident that the theory does not properly describe the shape of the spectrum. In particular, the lines at around −5 mm/s and +6 mm/s are much sharper than the experimental features. These lines (arrows) belong to the two

Table III. Exchange, Fine Structure, and Hyperfine Structure Parameters of the $Fe^{III}Ni^{II}$ Complex in Acetonitrile Solution[a]

J, cm^{-1}	D, cm^{-1}	E/D	A, MHz	$\lvert\Delta E_Q\rvert$, mm/s	δ, mm/s
+24 (3)	+0.7 (1)	0.32	−41.4 (5)	≤0.36	0.46 (3)

[a] Fine structure and hyperfine structure parameters pertain to the S = 3/2 multiplet, described by eqs 4, 7, and 10. We have used g = 2.0 in eq 4. Estimated uncertainties are given in parentheses. As described in the text, the parameter E/D is distributed.

electronic levels which become the "$M_S = \pm 1/2$" levels in the strong field limit. The outermost lines, on the other hand, belong to the "$M_S = \pm 3/2$" levels. At 0.4 T, the spin expectation values of the $M_S = \pm 1/2$ levels depend quite sensitively on D and E/D, while those of the $M_S = 3/2$ states are quite insensitive to variations of these parameters. Thus, if D and E/D are distributed, the spectral components associated with the $M_S = \pm 3/2$ levels will remain quite sharp, while those of the $M_S = \pm 1/2$ levels will broaden. In order to get a quantitative assessment, we have performed spectral simulations assuming that E/D is normally distributed with width $\sigma_{E/D}$ = 0.10 about its average E/D = 0.32. The simulation of Figure 11A shows the result of superimposing individual spectra over a Gaussian envelope. (In a "proper" coordinate frame, E/D can be restricted to $0 < E/D < 1/3$. Thus, for one-half of the distribution we have reversed the sign of D; this allows one to stay in the restricted range for E/D.) Although the simulation is not perfect, the simple distribution function describes the essential features of the data. Further improvement may be possible by considering a distribution for D as well.

We have studied the Mössbauer spectra up to a temperature of 160 K. At this temperature broad spectra, typical of intermediate relaxation rates, were observed. Therefore, we have estimated the quadrupole splitting from the 4.2 K magnetic data. We were able to determine that $|\Delta E_Q| < 0.30$ mm/s from a spectrum recorded in 50 mT transverse field. Since ΔE_Q is small, the data are quite insensitive to the electric field gradient tensor, and the asymmetry parameter η could not be determined; for the simulations we used η = 0.6.

Mössbauer Study of $[Fe^{III}Zn^{II}BPMP(OPr)_2](BPh_4)_2$. Information about the intrinsic properties of the Fe^{III} site is useful for analysis of the spin coupling of a dinuclear complex such as $[Fe^{III}Ni^{II}BPMP(OPr)_2](BPh_4)_2$. $Fe^{III}Zn^{II}BPMP(OPr)_2(BPh_4)_2$, where Ni^{II} is replaced by the diamagnetic Zn^{II}, provides a useful compound of reference. The EPR spectra of this complex in frozen acetonitrile solution show a broad resonance centered at g = 4.3. Mössbauer spectra recorded at 1.4 and 4.2 K in an applied field of 50 mT indicate high-spin Fe^{III}, with zero-field parameters 0.2 cm^{-1} < D < 0.5 cm^{-1} and $0.2 < E/D < 0.33$. Both the EPR and Mössbauer spectra indicate extensive strain, i.e., the zero-field parameter D and E/D are distributed over the ranges indicated. The distributions do not appear to be describable by simple Gaussians. Furthermore, the spectral shapes were found to be solvent dependent, and the distributions of D and E/D seemed to be affected by freezing effects. Fortunately, the magnetic hyperfine coupling constant A is well-defined as testified by Mössbauer studies performed in strong applied fields.

Figure 12 shows a Mössbauer spectrum of the $Fe^{III}Zn^{II}$ complex in acetonitrile solution recorded at 4.2 K in a parallel field of 6.0 T. The solid line is a spectral simulation by using a spin Hamiltonian appropriate for Fe^{III}, i.e., eqs 1 and 7 for $J = D_2 = g_2 = 0$, and $S_1 = 5/2$. From these simulations we obtained A_1 = −29.5 (2) MHz, δ = 0.43 (3) mm/s, $\Delta E_Q \simeq 0.5$ mm/s, and η = 1.[35]

(35) For 0.2 cm^{-1} < D < 0.5 cm^{-1} and H = 6.0 T the expectation values ⟨S⟩ are solely determined by the electronic Zeeman term. Since the Zeeman interaction and the magnetic hyperfine interaction are isotropic for high-spin Fe^{III}, nuclear $\Delta m = 0$ transitions are quenched for the spectrum of Figure 11. The presence of lines at −4 mm/s and +5 mm/s seems to indicate only partial quenching and one might conclude that D may be larger than quoted. However, the indicated two lines are, in fact, the outer lines of the Mössbauer spectrum associated with the $M_S = -3/2$ state which is populated to about 11% under the experimental conditions. The sharpness of the absorption lines implies that the anisotropy of the A tensor cannot exceed ±1%.

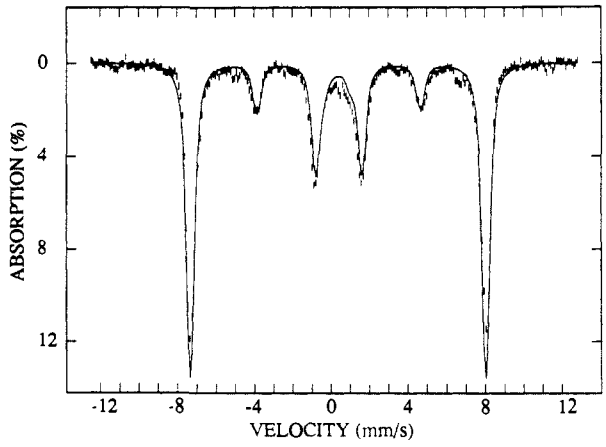

Figure 12. Mössbauer spectrum of a 5 mM solution of ^{57}Fe-enriched $[Fe^{III}Zn^{II}BPMP(OPr)_2](BPh_4)_2$. The spectrum was recorded at $T = 4.2$ K in a parallel applied field of 6.0 T. The solid line is a simulated spectrum using an $S = 5/2$ spin Hamiltonian with $A(Fe^{III}) = -29.5$ MHz for the magnetic hyperfine coupling constant. For details see text.

Conclusions

We have studied here the low-lying electronic states of $[Fe^{III}Ni^{II}BPMP(OPr)_2](BPh_4)_2$ with Mössbauer and EPR spectroscopy and magnetic susceptibility. Our studies show that the complex contains a high-spin ferric site which is antiferromagnetically coupled to a high-spin Ni^{II}. The coupling constant, $J = +24$ cm^{-1}, was determined by measuring the temperature dependence of an EPR signal associated with an excited state $S = 5/2$ manifold. To our knowledge, this is the first time that a J value has been determined for an iron-containing cluster by excited-state EPR spectroscopy. Within the uncertainties, we have obtained the same value for J from a magnetic susceptibility study.

The EPR spectrum of the ground manifold exhibits a resonance characteristic of an $S = 3/2$ state. The broad low field resonances testify that the ligand environment gives rise to electronic parameters, namely D and E/D, that are spread over a substantial range of values. The good fit to the Mössbauer spectrum of Figure 11A shows that the essential features of the distribution in E/D can be described by a Gaussian. On the other hand, we have found that the E/D strain observed with Mössbauer and EPR spectroscopy for $Fe^{III}Zn^{II}BPMP$ appears not to be describable by a simple symmetric distribution (data not shown). We wish to stress that all $Fe^{III}M^{II}$ BPMP complexes (M = Fe, Ni, Cu, Mn) which we have examined exhibit strains at low temperatures. In fact, we frequently screen a variety of solvents in order to obtain samples which exhibit minimal strain effects. It is not surprising that the frozen solution data exhibit distributions in some of the electronic parameters. Since the ligands of the two metal sites are in intimate contact with the lattice of the frozen solvent, strains occurring at the interface are probably readily transmitted to the metals. Not surprisingly, we have observed sharper Mössbauer features for polycrystalline materials. However, the high magnetic concentration of paramagnetic species in the solid leads to spin–spin interactions and, in some cases, long-range magnetic order which impedes EPR and low field Mössbauer studies. It is interesting to note that the magnetic hyperfine coupling constants A of the Fe^{III} sites are not observably affected by these strains; the sharp lines of the 6.0-T spectrum of Figure 10B constrain A to within ±1% of its mean value. This high attainable precision in the determination of A allows one to evaluate the magnetic hyperfine interactions reliably with a spin coupling model. It is also interesting to note that the A value of the $Fe^{III}Ni^{II}$ complex, $A_1 = {}^5/_7A = -29.6$ MHz, matches perfectly the A value of the noncoupled site of $Fe^{III}Zn^{II}$ complex, $A(Fe^{III}) = -29.5$ MHz, showing that the exchange interactions within the dinuclear complex leave the electronic structure of the local sites quite unaffected.

By combining the EPR and Mössbauer data, we can obtain through relation (5) some information about the local g values of the Ni^{II}. Unfortunately, the $g = 5.1$ resonance is quite broad, in part because the parameter E/D is distributed and perhaps in part because of unresolved hyperfine splittings. However, as pointed out above, the shape of this resonance does not change between 2 and 6 K, nor did we observe any changes in the 50-mT Mössbauer spectra between 1.4 and 4.2 K. This observation suggests that both Kramers doublets of the $S = 3/2$ multiplet have essentially the same effective g values at $E/D = 1/3$. The diagram of Figure 5 was drawn with the assumption that g as defined in eq 4 is isotropic, with $g_x = g_y = g_z = 2.00$. Our spectral simulations of Figure 6B show that g_z and g_y of eq 4 need to be lowered for a proper description of the $g' = 5.1$ resonance. A good match at $g' = 5.1$ was obtained for $g_y = g_z = 1.86$ and $g_x = 2.00$ (The spectrum is insensitive to g_x.) From this we estimate from eq 5 the values g_y (Ni^{II}) = g_z(Ni^{II}) = 2.35.

It can be seen from eq 6 that the zero-field splitting of the $S = 3/2$ multiplet would reflect essentially the zero-field splitting of the Fe^{III} site, if D_1 and D_2 had the same magnitude. However, since D_1 is quite small, as indicated by the data obtained for the $Fe^{III}Zn^{II}$ complex, the zero-field splitting of the Ni^{II} might contribute measurably to the value quoted for D. Susceptibility studies of a $Ga^{III}Ni^{II}$ analogue could furnish good estimates for the g and D values of the Ni^{II} site. It is also attractive to perform ENDOR studies on the ^{61}Ni-enriched $Fe^{III}Ni^{II}$ complex because such measurements may provide the rare opportunity to obtain the A tensor for a Ni^{II} site. Current research in our laboratories is aimed at furnishing this information.

Acknowledgment. We thank Prof. J. D. Britton for his generous help in solving the structure of the FeNi complex and Dr. E. P. Day for providing expertise and assistance for the susceptibility study. This work has been supported by the National Institutes of Health through Grants GM38767 (L.Q.) and GM22701 (E.M.), postdoctoral fellowship GM12996 (M.P.H.), and predoctoral traineeship GM08277 (T.R.H.).

Supplementary Material Available: Tables of atomic coordinates, bond lengths, bond angles, anisotropic thermal parameters, and calculated hydrogen atom positions (28 pages). Ordering information is given on any current masthead page.